Geochemical Perspectives Letters

# Geochemical evolution of melt/peridotite interaction at high pressure in subduction zones

**N. Malaspina, G. Borghini, S. Zanchetta, L. Pellegrino, M. Corti, S. Tumiati,**

## Supplementary Information

The Supplementary Information includes:

- S. 1 Microstructural Description of Peridotites and Websterite-Tremolitite of the Borgo outcrop
- S. 2 Analytical Techniques
- S. 3 Geochemical Modelling
- S. 4 Thermodynamic Modelling
- Tables S-1 to S-3
- Figures S-1 to S-6
- Supplementary Information References

## S. 1 Microstructural Description of Peridotites and Websterite-Tremolitite of the Borgo Outcrop

Chl-peridotites show a porphyroclastic structure (Fig. S-1a) characterised by coarse olivine ($Ol_1$), orthopyroxene ($Opx_1$), rarely preserved clinopyroxene ($Cpx_1$) and garnet completely substituted by chlorite ($Chl_1$; Fig. S-1b) during a HP hydration event that crystallised relict pargasitic to edenitic amphibole ($Amp_1$) and yielded to the partial melting of the associated eclogites (see Pellegrino *et al*., 2020). The interaction with eclogite-sourced melts and the Grt-Chl-peridotite at HP produced a porphyroblastic assemblage made of poikilitic orthopyroxene ($Opx_{porph}$) including $Ol_1$ (Fig. S-1c), amphibole ($Amp_{porph}$) and phlogopite ($Phl_{porph}$) postdating the original Grt-peridotite assemblage. Thermodynamic modelling indicates that the interaction between the eclogitic melt, and the surrounding Grt-Chl-peridotite likely produced layers of Grt-websterites (now retrogressed into tremolitites) constituted by Opx, Cpx, Grt and Hbl (Pellegrino *et al*., 2020). The first stage of decompression produced a finer grained recrystallised matrix of $Ol_2$, $Opx_2$, pargasitic to edenitic amphibole ($Amp_2$) and spinel ($Spl_2$) in the peridotites (Fig. S-1d) and crystallised Hbl in the Grt-websterites (Fig. S-1e).

After the decompression, a LP-(U)HT event has been recorded by Grt-peridotites of Mt. Duria and Borgo eclogites, with crystallisation of symplectitic $Opx_{sym}$, $Cpx_{sym}$, pargasitic $Amp_{sym}$, $Sp_{sym}$, Spr + Bdy + Sri around garnet in the peridotites (Tumiati *et al*. 2018) and Spr+Crn around kyanite in the eclogites (Tumiati *et al*. 2018). In those samples of Borgo peridotites close to the contact with the eclogitic migmatite, chlorite ($Chl_3$) and tremolitic to edenitic amphibole ($Amp_3$) are aligned along a pervasive foliation (Fig. S-1d), indicative of a late-stage LP-LT hydration event, that

substitute all the previous mineral parageneses. This hydration event transformed the Grt-websterites into tremolitites, showing relict of coarse Mg-hornblende (Hbl), surrounded by a fine-grained and mosaic like matrix of tremolite ($Tr_1$) overgrown by a second generation of mm-sized $Tr_2$ (Fig. S-1e). The samples closed to the contact between eclogitic migmatite and Chl-peridotite show Tr + Phl + Tlc + Chl pseudomorphs after garnet (Fig. S-1f). A summary of the mineral parageneses reconstructed in Chl-peridotites and tremolitites is reported in Table S-2.

## S. 2 Analytical Techniques

Major and trace elements whole-rock analyses were performed by inductively coupled plasma mass spectrometry (ICP-MS) and LECO combustion (total C, S) at Bureau Veritas ACME Mineral Laboratories, Canada. Results are reported in Table S-3.

## S. 3 Geochemical Modelling

We use the "Plate Model" proposed by Vernières *et al*. (1997) to simulate the REE gradient shown by the tremolitite veins sampled within the first 30 meters of peridotite from the eclogite-peridotite contact (see profile in Fig. 1). The numerical simulation reproduces a rock-dominated system where the solid matrix, varying in porosity and in modal composition along the percolation column, buffers the composition of the infiltrating melt. In our case, the profile through the peridotites containing the tremolitite veins represents the mantle column that we ideally divide in meter-scale portions ("cells") of peridotite infiltrated by the same melts. Note that the cell-1 is adjacent to the source of infiltrating melt, *i.e*., peridotite-eclogite interface, whereas the number of cells increases going furthest away. The composition of liquids resulting from calculation is here assumed to form veins of Grt-websterites (see also thermodynamic modelling) that are therefore the protoliths of tremolitites that still preserve their original bulk REE composition. We approximate the REE composition of liquid to the REE abundance of pyroxenites embedded in Borgo peridotite at variable distance from the eclogite-peridotite contact.

The initial solid matrix is the DMM of Salters and Stracke (2004) having a Grt-lherzolite mode of Ol:Opx:Cpx:Grt = 0.60:0.25:0.12:0.03. The REE compositions of olivine, orthopyroxene, clinopyroxene and garnet are calculated assuming equilibrium with the REE composition of DMM, using partition coefficients by Salters *et al*. (2002). Normalising values are from McDonough and Sun (1995). Our model assumes the eclogite-derived leucosome DB131 composition (Pellegrino *et al*., 2020) as starting percolating melt.

The geochemical model includes two steps of melt-peridotite reaction: *first step* (Step1) assumes high peridotite assimilation step (*i.e.,* high $M_a/M_c$ ratio, where $M_a$ is the mass of assimilated peridotite and $M_c$ is the mass of crystallised melt) at crust-mantle boundary and it is followed by a *second step* (Step2) of reacted melt percolation within the adjacent peridotite assuming variable amounts of olivine assimilation and pyroxene + garnet (+ amphibole or phlogopite) crystallisation. The *first step* (Step1) simulates the interaction of eclogite-derived melt (DB131) with peridotite (DMM) at the peridotite-eclogite interface, assuming an initial porosity of 0.1 in the peridotite, high extent of peridotite assimilation and low rate of clinopyroxene + garnet crystallisation (0.6 and 0.4 respectively). This step generates a final liquid with REE composition that well reproduces the pyroxenite vein DB177 sampled at the eclogite-peridotite contact (see Fig. 2a). We obtained a comparable result by replicating the calculation using the *adakite2* from Corgne *et al*. (2018), as initial reacting melt (Fig. S-6a). Although garnet and clinopyroxene are the main minerals expected to crystallize from an eclogite-derived melt at about 2 GPa (Pertermann and Hirschmann, 2003; Wang *et al*., 2020), orthopyroxene can be also precipitated as a result of reaction with the peridotite (Rapp *et al*., 2010, Wang *et al*., 2020; see also Fig. S-5). Nevertheless, the model shows that at high $M_a/M_c$ ratio the addition of variable amount (30 or 50%) of orthopyroxene (having rather low $K_d$ for the REEs) in the crystallizing assemblage does not impact significantly on the melt REE composition resulting from the reaction (Fig.S-6b). We also evaluated the role of variable extent of initial porosity: Figure S-6b shows that porosity higher than 0.1 fails to reproduce the low $La_N/Sm_N$ of melt that generated the

retrogressed Grt-websterite (DB177) close to the contact with the peridotite-eclogite interface. On contrary, assuming porosity lower than 0.1 the model results in too fast melt $La_N/Sm_N$ lowering.
In the *second step* (Step2), our model simulates the reactive melt percolation through the first 36 meters of peridotite from the crust-mantle contact as described in the profile of Figure 1b. We assume a relatively high instantaneous melt/peridotite ratio (*i.e.*, initial porosity of 0.2, which reflects the high peridotite assimilation of the Step1; Fig. S-6b) combined with high extents of fractional crystallisation and very low mass assimilation ($M_a/M_c$ ratio of 0.56-0.61), which result in a rapid decrease of melt mass at increasing interaction cells. The choice of this combination of parameters is justified by a scenario of reactive melt percolation from a melt source at slab-mantle interface, explaining the relatively high initial porosity, coupled to the progressive melt consumption through melt-peridotite reaction during the percolation (*i.e.*, high extent of transient melt crystallisation), which is here simulated by the progressive increase of the crystallisation rate. As starting reacting melt, we used the REE composition of the liquid resulting after the first step, *i.e.*, the liquid with the lowest REE abundance in Figure 2a (see also Fig. 3). We performed the second step of the model by assuming initial and final crystallization of pyroxenes and garnet (four-phase calculation; 0.6 Opx, 0.2 Cpx, 0.2 Grt). The mode of crystallisation assemblage has been derived by the thermodynamic modelling of eclogite melt/peridotite interaction (Fig. S-5; Section S.4 of the Supplementary Material). Other calculations also include amphibole or phlogopite (five-phase calculation; see the crystallisation modes in the caption of Fig. S-6c,d: 0.5 Opx, 0.2 Cpx, 0.2 Grt, 0.1 Amp/Phl)). The highest LREE and MREE enrichment is produced by the fractional crystallisation of pyroxenes and garnet, whereas the involvement of amphibole or phlogopite results in a moderate REE increment (*c.f.* Fig. 2b and Fig. S-6c,d). REE partition coefficients for amphibole and phlogopite are from Ionov *et al*. (2002) and Corgne *et al*. (2018), respectively. Olivine is always the dissolving phase. Results in terms of liquid REE patterns are reported in Figure 2b and 3. They account for the REE gradient, *i.e.*, the overall increase of REE abundance and LREE-HREE fractionation ($Ce_N/Yb_N$), observed in the retrogressed Grt-websterite (now tremolitite) bulks within the first 30 m of peridotite.

## S. 4 Thermodynamic modelling

Thermodynamic modelling shown in Figure S-5 is performed with the software package Perple_X (http://www.perplex.ethz.ch; Connolly, 2005), using the thermodynamic database of Holland and Powell (1998) revised in 2002 (hp02ver.dat), and the following solution models described in Holland and Powell (1998) (HP), Diener and Powell (2012) (DP), Holland and Powell (2003) (I1,HP), and White *et al*. (2014) (W): Gt(HP) for garnet, Opx(HP) for orthopyroxene, O(HP) for olivine, Omph(HP) for clinopyroxene, Chl(W) for chlorite, Sp(HP) for spinel, Pheng(HP) for white mica, Bio(HP) for phlogopite, Pl(I1,HP) for ternary feldspars, cAmph(DP) for amphibole. The equation of state of water is taken from Holland and Powell (1998). Aim of the modelling was to estimate the modal composition of Grt-websterites before the LP hydration event resulting from the interaction between Grt-peridotite and the eclogite leucosome at peak conditions (3 GPa, 750 °C). Results indicate that the volume proportions of the hybrid websterite at X = 0.2 weight fraction and $\log a_{H2O}$ = -0.2 are: Opx 43.66 %, Ol 25.05 %, Grt 11.61 %, Cpx 12.96 % and Phl 6.72 %. This modal composition, normalised without olivine, has been used to estimate the modal mineral composition crystallised in the Step2 of the geochemical model resulting in Figure 2b.

# Supplementary Tables

**Table S-1**

Sample distance from the contact, mineral association, and microstructure of the studied profile. See Table S-2 for minerals generations. An Excel version of Table S-1, is available for download from the online version of this article at https://doi.org/10.7185/geochemlet.2305

**Table S-2**

Mineral parageneses reconstructed in Chl-peridotites and tremolitite layers of Borgo. The HP and LP-HT metamorphic event is from Pellegrino *et al.* (2020) and *Tumiati *et al.* (2018) respectively. An Excel version of Table S-2, is available for download from the online version of this article at https://doi.org/10.7185/geochemlet.2305

**Table S-3**

Bulk rock major (oxide wt. %) and trace elements (µg/g) composition. bdl = below detection limit. An Excel version of Table S-3, is available for download from the online version of this article at https://doi.org/10.7185/geochemlet.2305

## Supplementary Figures

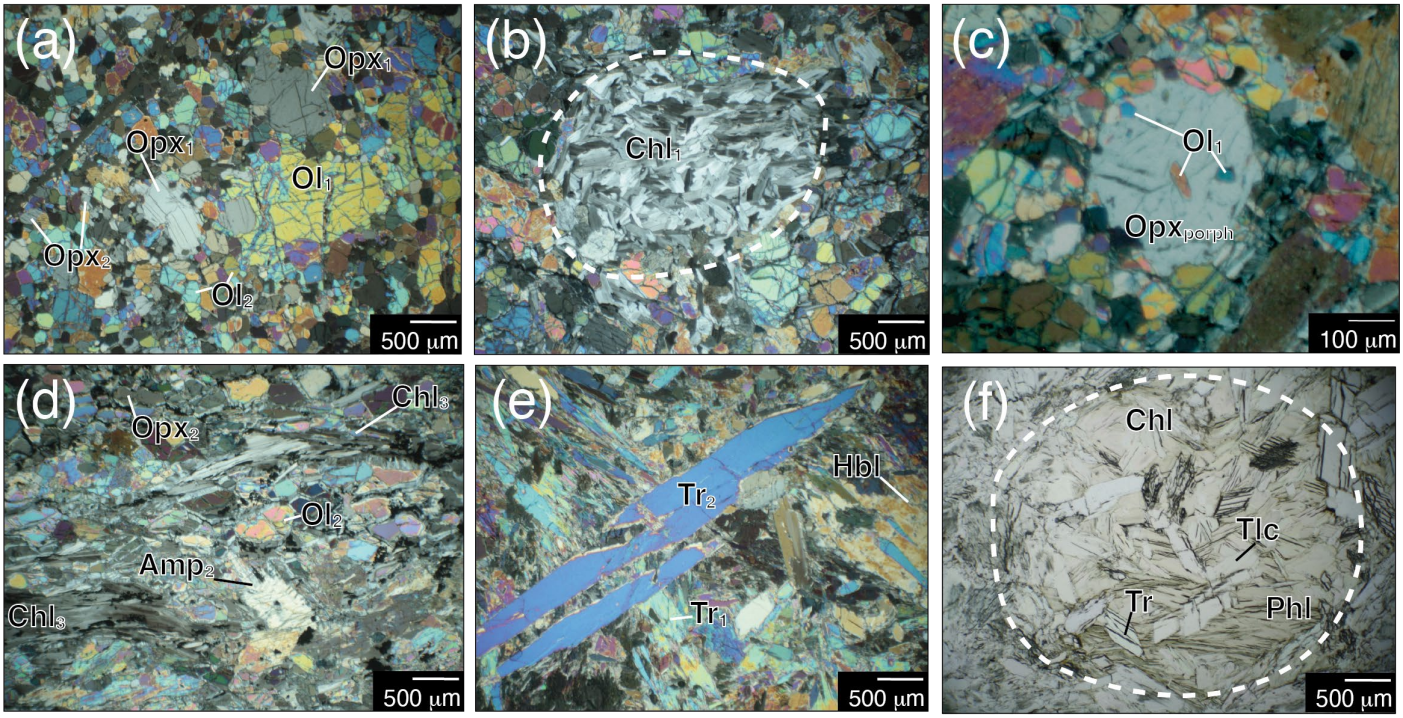


**Figure S-1** Crossed polarised photomicrograph of retrogressed Grt-peridotite showing **(a)** two generations of Ol + Opx; **(b)** garnet completely substituted by chlorite ($Chl_1$); **(c)** metasomatic orthopyroxene ($Opx_{porph}$) growing at the expenses of olivine; **(d)** $Amp_2$ in equilibrium with $Ol_2$ and $Opx_2$ wrapped by a late-stage pervasive foliation of $Chl_3$. Crossed and plane polarised photomicrograph of retrogressed Grt-websterite (tremolitite) showing **(e)** relict Hbl overgrown by two Tr generations; **(f)** Phl + Chl + Tr + Tlc pseudomorph after garnet.

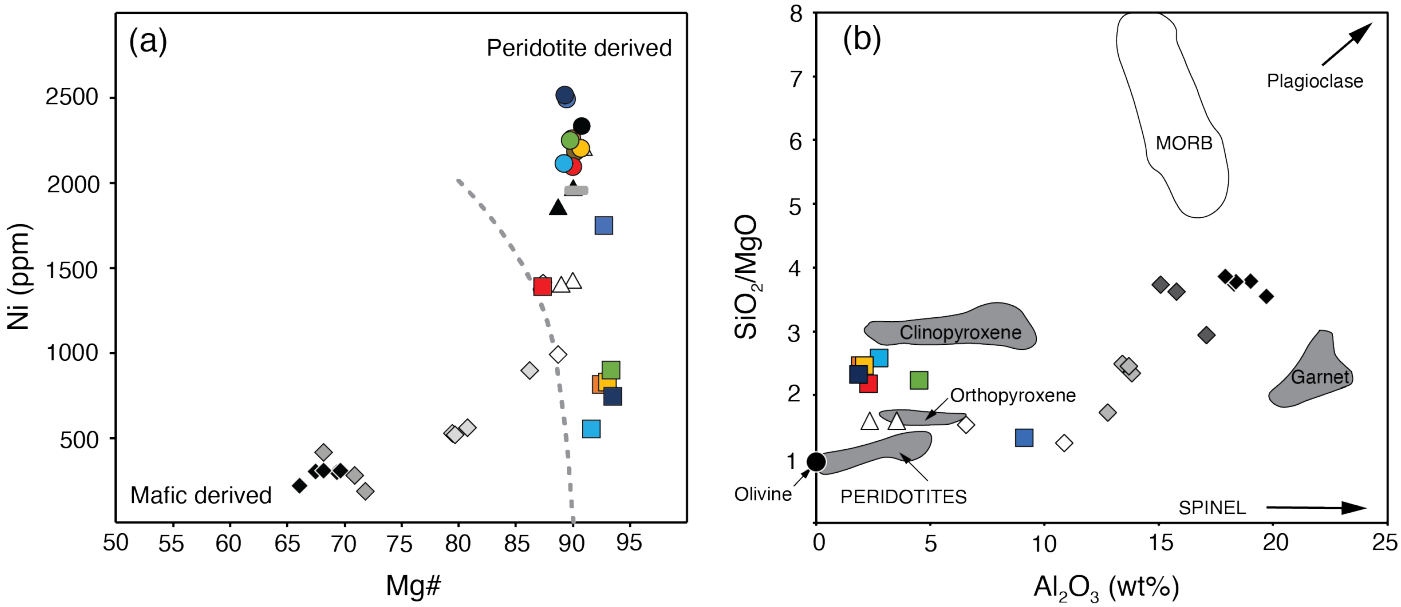


**Figure S-2 (a)** Mg# versus Ni plot of Chl-peridotite (coloured circles) and tremolitite (coloured squares) from Borgo (colours are the same as Fig. 3 and Fig. S-3). The dashed grey curve represents the possible transition from mafic to ultramafic derived rocks. **(b)** $SiO_2$/MgO versus $Al_2O_3$ of tremolitites from Borgo. The MORB array (white area) and the compositions of olivine (89% forsterite), orthopyroxene, clinopyroxene, and garnet in mafic rocks from orogenic peridotites (grey areas) are from Bodinier and Godard (2014) and references therein. Grt-peridotites from Mt. Duria (black triangles; Pellegrino *et al.*, 2020), Grt-pyroxenites (type A, black diamonds; type B, dark grey diamonds) and Sp-pyroxenites (type I, light grey diamonds; type II, white diamonds) from External Ligurides (Montanini *et al.*, 2012), UHP Grt-orthopyroxenites and websterites from Dabie Shan (white triangles; Malaspina *et al.*, 2006) and reference Depleted Mantle (grey solid line; Salters and Stracke, 2004) are also reported for comparison.

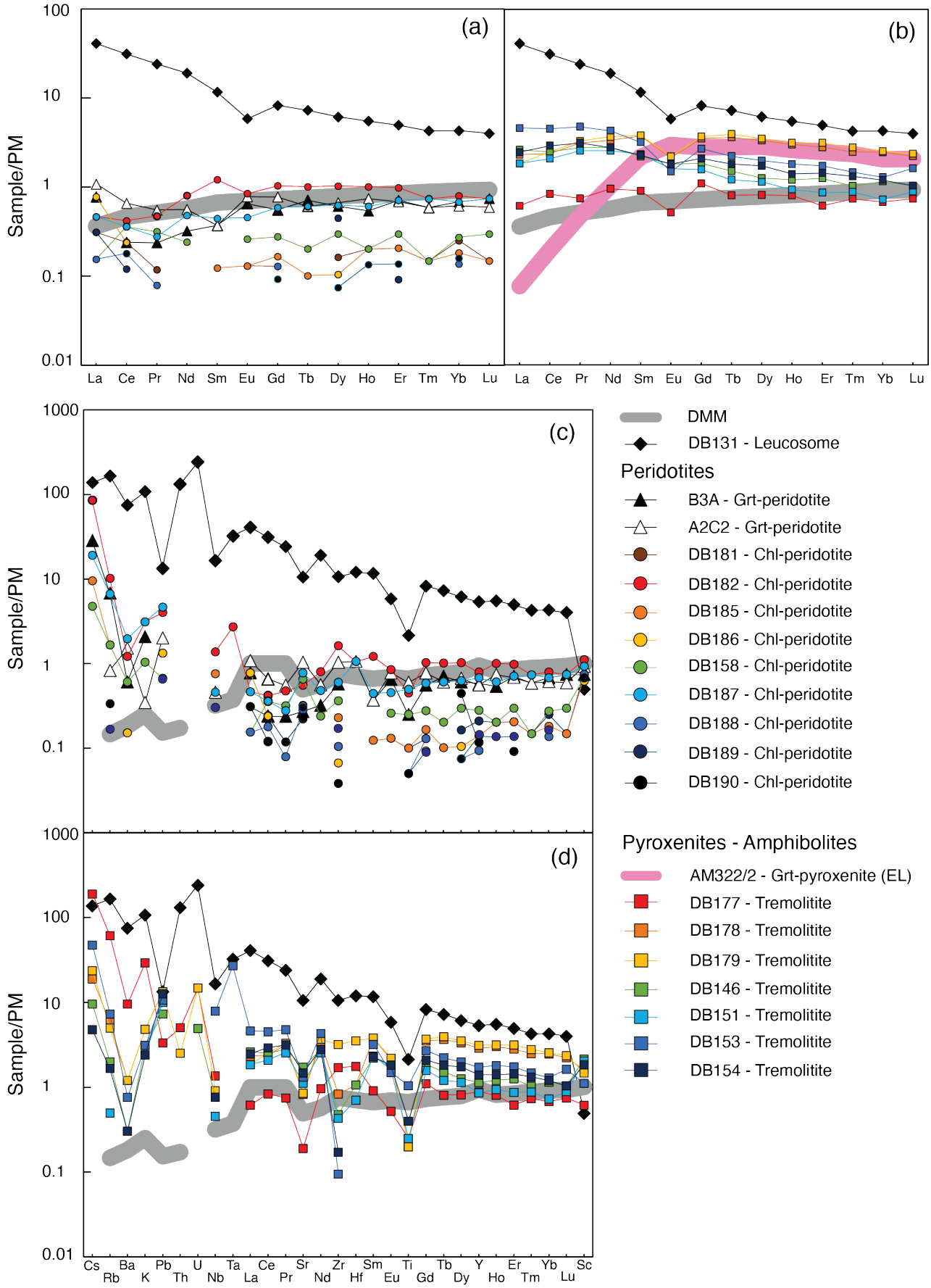
(a)
(b)
(c)
(d)
Sample/PM
100
10
1
0.1
0.01
1000
La Ce Pr Nd Sm Eu Gd Tb Dy Ho Er Tm Yb Lu
Cs Rb Ba K Pb Th U Nb Ta La Ce Pr Sr Nd Zr Hf Sm Eu Ti Gd Tb Dy Y Ho Er Tm Yb Lu Sc
DMM
DB131 - Leucosome
Peridotites
B3A - Grt-peridotite
A2C2 - Grt-peridotite
DB181 - Chl-peridotite
DB182 - Chl-peridotite
DB185 - Chl-peridotite
DB186 - Chl-peridotite
DB158 - Chl-peridotite
DB187 - Chl-peridotite
DB188 - Chl-peridotite
DB189 - Chl-peridotite
DB190 - Chl-peridotite
Pyroxenites - Amphibolites
AM322/2 - Grt-pyroxenite (EL)
DB177 - Tremolitite
DB178 - Tremolitite
DB179 - Tremolitite
DB146 - Tremolitite
DB151 - Tremolitite
DB153 - Tremolitite
DB154 - Tremolitite

**Figure S-3** Primitive Mantle (PM) normalised REE and other trace element patterns of the investigated samples (data from Table S-3). Elements are presented in order of increasing compatibility (left to right) during melting in the upper mantle (Hofmann, 1988; Sun and McDonough, 1989). Normalising values are from McDonough and Sun (1995). **(a)** REE patterns of Grt-peridotites from Mt. Duria (triangles; Pellegrino *et al*., 2020) and Chl-peridotites from Borgo (coloured circles), compared with eclogite leucosome (black diamonds; Pellegrino *et al*., 2020) and reference Depleted MORB Mantle (grey solid line DMM; Salters and Stracke, 2004). **(b)** REE patterns of tremolitites from Borgo (coloured squares) compared with eclogite leucosome DB131 and Grt-pyroxenite from External Ligurides (EL, pink solid line AM322/2; Montanini *et al*., 2012). **(c, d)** Trace elements patterns of Grt-peridotites and tremolitites, respectively, compared with eclogite leucosome DB131 and DMM.

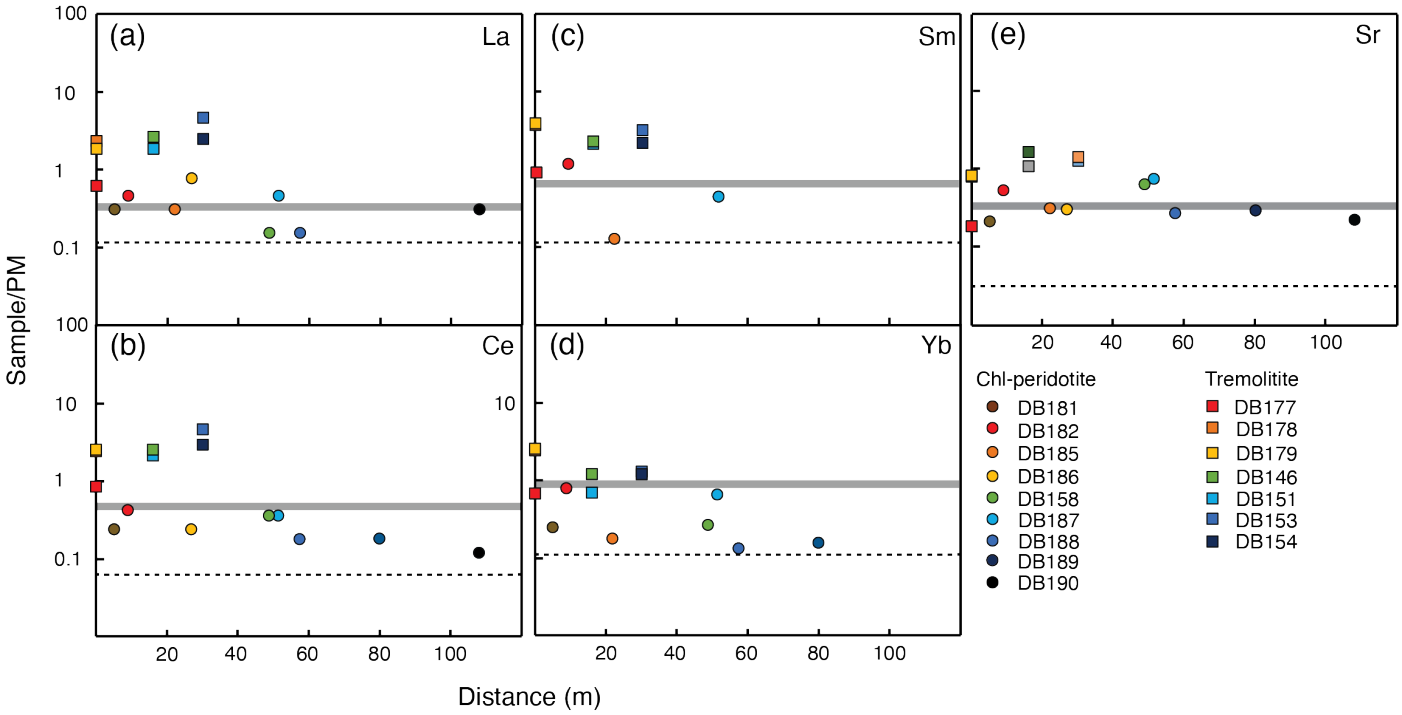


**Figure S-4** Primitive Mantle normalised selected LREE **(a,b)** MREE **(c)** HREE **(d)** fluid mobile elements **(e)** of Chl-peridotites and tremolitites from Borgo along a 120 m length section starting from the contact with migmatised eclogites. The grey line is the reference DMM of Salters and Stracke (2004); the black dashed line is the analytical detection limit. Normalising values are from McDonough and Sun (1995).

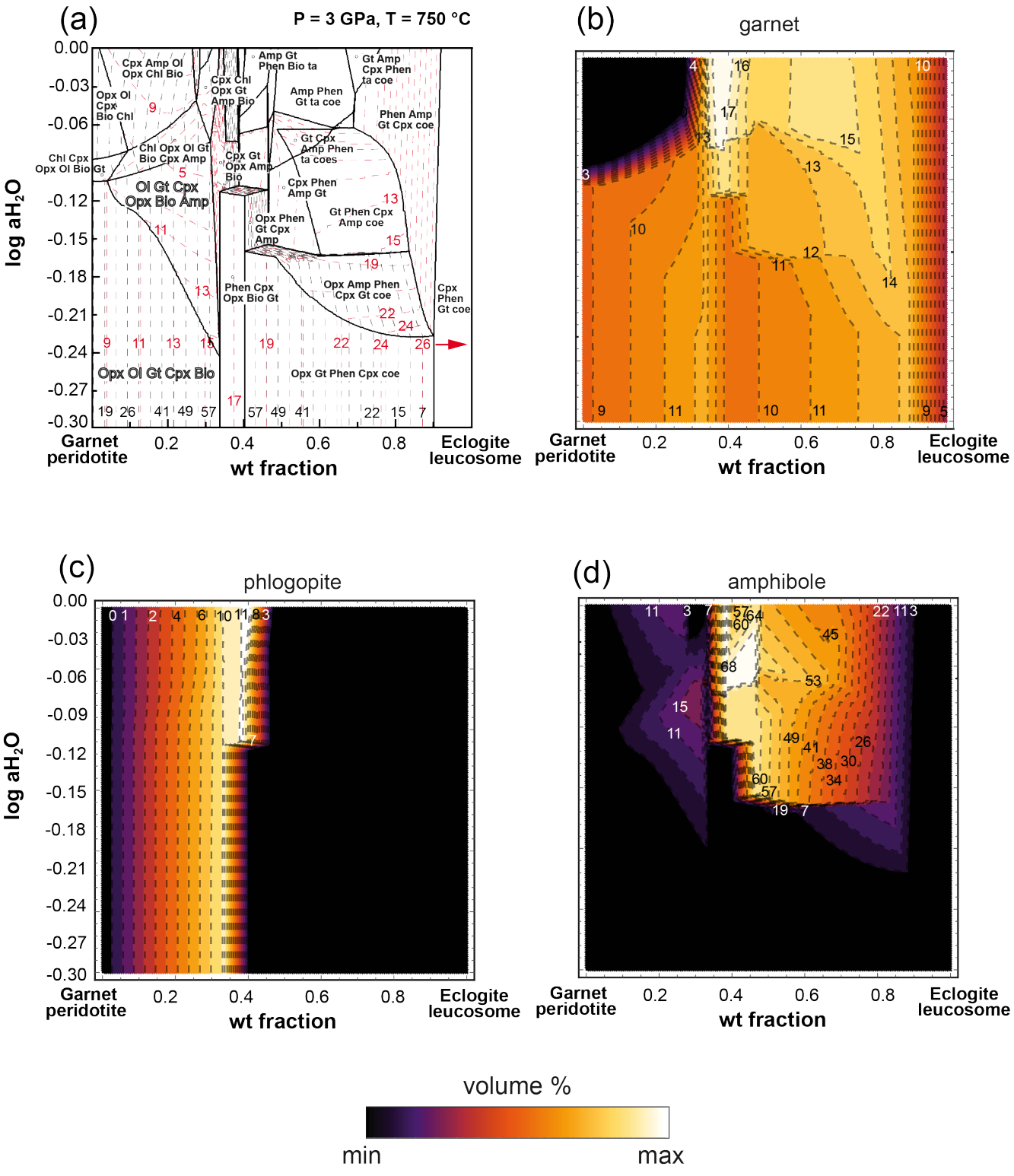
(a)
P = 3 GPa, T = 750 °C
log aH2O
wt fraction
Garnet peridotite
Eclogite leucosome
Cpx Amp Ol Opx Chl Bio
Amp Gt Phen Bio ta
Gt Amp Cpx Phen ta coe
Opx Ol Cpx Bio Chl
Cpx Chl Opx Gt Amp Bio
Amp Phen Gt ta coe
Phen Amp Gt Cpx coe
Chl Cpx Opx Ol Bio Gt
Chl Opx Ol Gt Bio Cpx Amp
Cpx Gt Opx Amp Bio
Gt Cpx Amp Phen ta coes
Ol Gt Cpx Opx Bio Amp
Cpx Phen Amp Gt
Gt Phen Cpx Amp coe
Opx Phen Gt Cpx Amp
Phen Cpx Opx Bio Gt
Opx Amp Phen Cpx Gt coe
Cpx Phen Gt coe
Opx Ol Gt Cpx Bio
Opx Gt Phen Cpx coe
(b)
garnet
(c)
phlogopite
(d)
amphibole
volume %
min
max

**Figure S-5 (a)** log $aH_2O$–X diagram calculated at fixed P = 3 GPa and T = 750 °C for garnet websterite forming after the melt-peridotite reaction. X = 0 corresponds to garnet peridotite (A2C2; Pellegrino *et al*., 2020), while X = 1 corresponds to the bulk of eclogite leucosome (DB131; Pellegrino *et al*., 2020). Dashed lines and corresponding numbers are the isomodes (vol%) of orthopyroxene (black) and clinopyroxene (red). **(b, c, d)** same log $aH_2O$–X diagram as shown in (a) reporting the isomodes (vol%) of garnet, phlogopite and amphibole respectively.

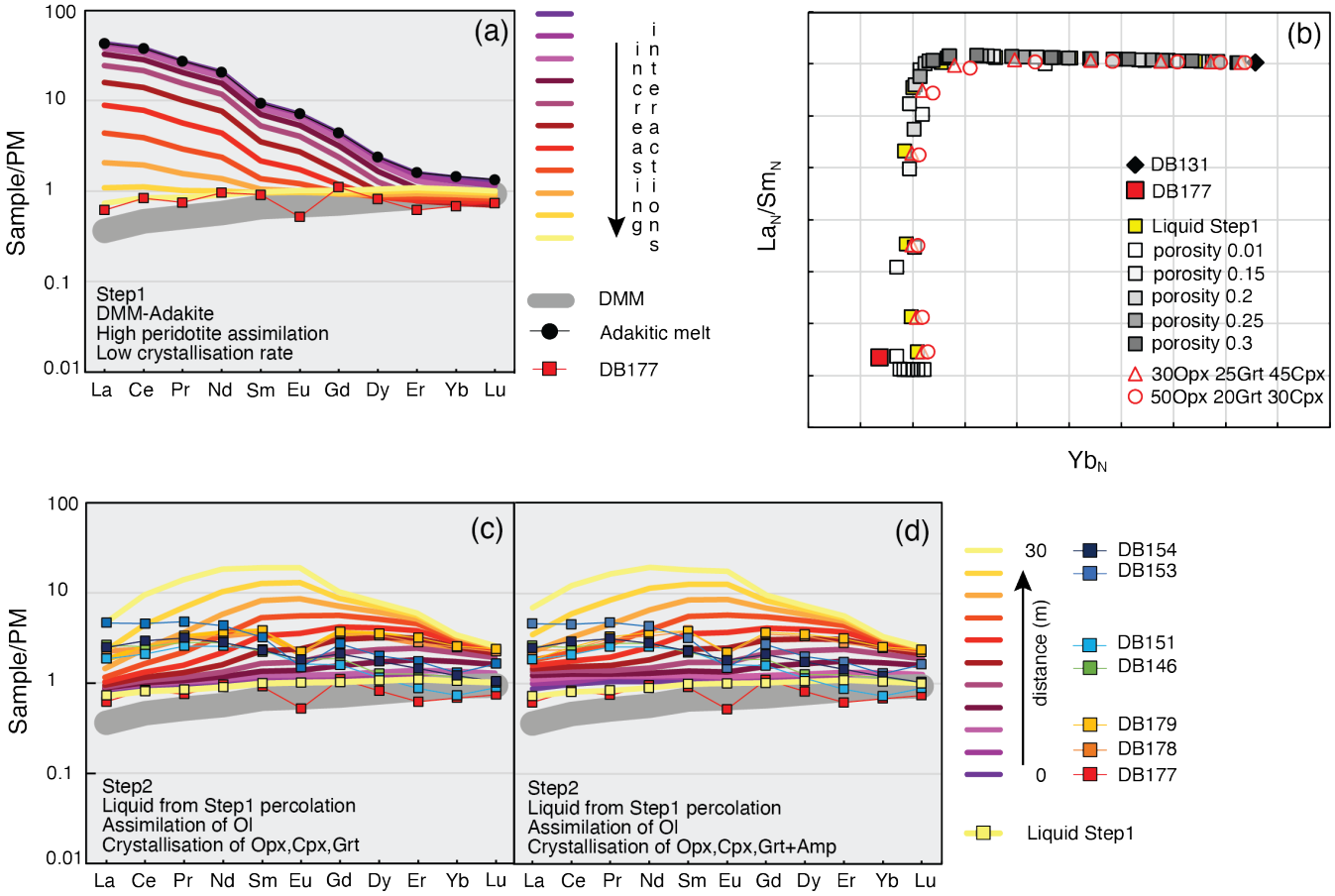


**Figure S-6** Numerical simulation of melt-rock interaction at slab-mantle interface and reactive percolation of melt through mantle peridotite using Plate Model. **(a)** PM-normalised REE patterns of the liquid resulting from melt-peridotite interaction (Step1), using the same parameters as in Figure 2, but assuming as initial reacting melt the *adakite2* from Corgne *et al.* (2018). **(b)** PM-normalised Yb vs La/Sm of melt resulting from the percolation of the liquid after Step1 at variable porosity (squares) and 30% or 50% of orthopyroxene (triangles and circles) in the crystallizing assemblage. **(c, d)** Evolution of PM normalised REE abundances in the liquid originated by reactive percolation of reacted melt after Step1 through the DMM peridotite. Model assumes a high infiltrating melt amount (*i.e.*, starting porosity of 20%), low assimilation of olivine and high extent with the following modes: (c) 30% Cpx, 30% Opx and 40% Grt; (d) 50% Opx, 20% Cpx, 20% Grt and 10% Amp. Patterns with coloured squares (except light yellow) are the REE bulk compositions of tremolitites sampled in the Borgo outcrop within the first 30 meters from the migmatitic eclogite-peridotite contact (see Fig. 1). Coloured lines refer to the progressive cells of the model.

# Supplementary Information References


Bodinier, J.L., Godard, M. (2014) Orogenic, Ophiolitic, and Abyssal Peridotites. *Treatise on Geochemistry (Second Edition)*, Elsevier, 2014, Pages 103-167. https://doi.org/10.1016/B978-0-08-095975-7.00204-7.

Connolly, J.A.D. (2005) Computation of phase equilibria by linear programming: A tool for geodynamic modeling and its application to subduction zone decarbonation. *Earth and Planetary Science Letters* 236, 524–541. https://doi.org/10.1016/j.epsl.2005.04.033

Corgne, A., Schilling, M.E., Grégoire, M., Langlade, J. (2018) Experimental constraints on metasomatism of mantle wedge peridotites by hybridized adakitic melts. *Lithos 308*, 213-226. https://doi.org/10.1016/j.lithos.2018.03.006

Diener, J.F.A., Powell, R. (2012) Revised activity-composition models for clinopyroxene and amphibole. *Journal of Metamorphic Geology* 30, 131–142. https://doi.org/10.1111/j.1525-1314.2011.00959.x

Hofmann, A.W. (1988) Chemical differentiation of the Earth: the relationship between mantle, continental crust and oceanic crust. *Earth and Planetary Science Letters* 90, 297–314. https://doi.org/10.1016/0012-821X(88)90132-X

Holland, T.J.B, Powell, R. (1998) An internally consistent thermodynamic data set for phases of petrological interest. *Journal of Metamorphic Geology* 16, 309-343. https://doi.org/10.1111/j.1525-1314.1998.00140.x

Holland, T.J.B., Powell, R. (2003) Activity–composition relations for phases in petrological calculations: an asymmetric multicomponent formulation. *Contributions to Mineralogy and Petrology* 145, 492–501. https://doi.org/10.1007/s00410-003-0464-z

Ionov, D.A., Bodinier, J.L., Mukasa, S.B., Zanetti, A. (2002) Mechanisms and sources of mantle metasomatism: major and trace element conditions of peridotite xenoliths from Spitzbergen in the context of numerical modelling. *Journal of Petrology* 43, 2219–2259. https://doi.org/10.1093/petrology/43.12.2219

Malaspina, N., Hermann, J., Scambelluri, M., Compagnoni, R. (2006) Polyphase inclusions in garnet-orthopyroxenite (Dabie-Shan, China) as monitors for metasomatism and fluid-related trace element transfer in subduction zone peridotite. *Earth and Planetary Science Letters* 249, 173–187. https://doi.org/10.1016/j.epsl.2006.07.017

McDonough, W.F., Sun, S.S. (1995) Composition of the Earth. *Chemical Geology* 120, 223–253. https://doi.org/10.1016/0009-2541(94)00140-4

Montanini, A., Tribuzio, R., Thirlwall, M. (2012) Garnet clinopyroxenite layers from the mantle sequences of the Northern Apennine ophiolites (Italy): Evidence for recycling of crustal material. *Earth and Planetary Science Letters* 351-352, 171–181. https://doi.org/10.1016/j.epsl.2012.07.033

Pellegrino, L., Malaspina, N., Zanchetta, S., Langone, A., Tumiati, S. (2020) High pressure melting of eclogites and metasomatism of garnet peridotites from Monte Duria Area (Central Alps, N Italy): A proxy for melt-rock reaction during subduction. *Lithos* 358-359, 105391. https://doi.org/10.1016/j.lithos.2020.105391

Pertermann, M., Hirschmann, M. M. (2003) Anhydrous partial melting experiments on MORB-like eclogite: phase relations, phase compositions and mineral–melt partitioning of major elements at 2–3 GPa. *Journal of Petrology* 44, 2173-220. https://doi.org/10.1093/petrology/egg074

Rapp, R.P., Norman, M.D., Laporte, D., Yaxley, G.M., Martin, H., Foley, S.F. (2010) Continent formation in the Archean and chemical evolution of the cratonic lithosphere: melt–rock reaction experiments at 3–4 GPa and petrogenesis of Archean Mg-diorites (sanukitoids). *Journal of Petrology* 51, 1237-1266. https://doi.org/10.1093/petrology/egq017

Salters, V.J.M., Longhi, J.M., Bizimis, M. (2002) Near mantle solidus trace element partitioning at pressures up to 3.4 GPa. *Geochemistry, Geophysics, Geosystems* 3, 1-23. https://doi.org/10.1029/2001GC000148

Salters, V.J.M., Stracke, A. (2004) Composition of the depleted mantle. *Geochemistry Geophysics Geosystems* 5. https://doi.org/10.1029/2003GC000597

Sun, S.S., McDonough, W.F. (1989) Magmatism in Ocean Basins Chemical and Isotopic Systematics of Ocean Basalts: Implications for Mantle Composition and Processes. *Geological Society of London, Special Publications* 42, 313-345. https://doi.org/10.1144/GSL.SP.1989.042.01.19

Tumiati, S., Zanchetta, S., Pellegrino, L., Ferrario, C., Casartelli, S., Malaspina, N. (2018) Granulite-facies overprint in garnet peridotites and kyanite eclogites of Monte Duria (Central Alps, Italy): clues from srilankite-and sapphirine-bearing symplectites. *Journal of Petrology* 59, 115-151. https://doi.org/10.1093/petrology/egy021

Vernières, J., Godard, M., Bodinier, J.L. (1997) A plate model for the simulation of trace element fractionation during partial melting and magma transport in the Earth's upper mantle. *Journal of Geophysical Research: Solid Earth*, 102, 24771-24784. https://doi.org/10.1029/97JB01946

Wang, C., Cascio, M.L., Liang, Y., & Xu, W. (2020) An experimental study of peridotite dissolution in eclogite-derived melts: implications for styles of melt-rock interaction in lithospheric mantle beneath the North China Craton. *Geochimica et Cosmochimica Acta* 278, 157-176. https://doi.org/10.1016/j.gca.2019.09.022

White, R.W., Powell, R., Johnson, E. (2014) The effect of Mn on mineral stability in metapelites revisited: New a–x relations for manganese-bearing minerals. *Journal of Metamorphic Geology* 16, 309-343. https://doi.org/10.1111/jmg.12095